Bandgap modulation in photoexcited topological insulator Bi2Te3 via atomic displacements

Masaki Hada, Katsura Norimatsu, Sei'ichi Tanaka, Sercan Keskin, Tetsuya Tsuruta, Kyushiro Igarashi, Tadahiko Ishikawa, Yosuke Kayanuma, R. J. Dwayne Miller, Ken Onda, Takao Sasagawa, Shin-ya Koshihara, and Kazutaka G. Nakamura

---

Articles you may be interested in

Electronic structure of a superconducting topological insulator Sr-doped Bi2Se3
Appl. Phys. Lett. **107**, 171602 (2015); 10.1063/1.4934590

Surface optical and bulk acoustic phonons in the topological insulator, Bi2Se2Te
Appl. Phys. Lett. **106**, 241106 (2015); 10.1063/1.4922641

Epitaxial growth of the topological insulator Bi2Se3 on Si(111): Growth mode, lattice parameter, and strain state
Appl. Phys. Lett. **103**, 111909 (2013); 10.1063/1.4821181

Simple tuning of carrier type in topological insulator Bi2Se3 by Mn doping
Appl. Phys. Lett. **101**, 152103 (2012); 10.1063/1.4755767

Surface versus bulk state in topological insulator Bi2Se3 under environmental disorder
Appl. Phys. Lett. **99**, 012109 (2011); 10.1063/1.3607484

Bandgap modulation in photoexcited topological insulator Bi$_2$Te$_3$ via atomic displacements

Masaki Hada,[1,2,3,a)] Katsura Norimatsu,[2] Sei′ichi Tanaka,[4] Sercan Keskin,[5]
Tetsuya Tsuruta,[2] Kyushiro Igarashi,[2] Tadahiko Ishikawa,[4] Yosuke Kayanuma,[2]
R. J. Dwayne Miller,[5,6] Ken Onda,[3,7] Takao Sasagawa,[2] Shin-ya Koshihara,[4]
and Kazutaka G. Nakamura[2]

[1]*Graduate School of Natural Science and Technology, Okayama University, Okayama 700-8530, Japan*
[2]*Materials and Structures Laboratory, Tokyo Institute of Technology, Yokohama 226-8503, Japan*
[3]*PRESTO, Japan Science and Technology Agency, Kawaguchi 332-0012, Japan*
[4]*Department of Chemistry and Materials Science, Tokyo Institute of Technology, Tokyo 152-8551, Japan*
[5]*The Max Planck Institute for the Structure and Dynamics of Matter, The Hamburg Centre*
for Ultrafast Imaging, University of Hamburg, Hamburg 22761, Germany
[6]*Departments of Chemistry and Physics, University of Toronto, Toronto M5S 3H6, Canada*
[7]*Graduate School of Science and Engineering, Tokyo Institute of Technology, Yokohama 226-8502, Japan*

The atomic and electronic dynamics in the topological insulator (TI) Bi$_2$Te$_3$ under strong photoexcitation were characterized with time-resolved electron diffraction and time-resolved mid-infrared spectroscopy. Three-dimensional TIs characterized as bulk insulators with an electronic conduction surface band have shown a variety of exotic responses in terms of electronic transport when observed under conditions of applied pressure, magnetic field, or circularly polarized light. However, the atomic motions and their correlation between electronic systems in TIs under strong photoexcitation have not been explored. The artificial and transient modification of the electronic structures in TIs via photoinduced atomic motions represents a novel mechanism for providing a comparable level of bandgap control. The results of time-domain crystallography indicate that photoexcitation induces two-step atomic motions: first bismuth and then tellurium center-symmetric displacements. These atomic motions in Bi$_2$Te$_3$ trigger 10% bulk bandgap narrowing, which is consistent with the time-resolved mid-infrared spectroscopy results. *Published by AIP Publishing.* [http://dx.doi.org/10.1063/1.4955188]

I. INTRODUCTION

Three-dimensional topological insulators (TIs) which are characterized as bulk insulators with an electronic-conduction surface band[1–4] have yielded a variety of exotic electronic-transport responses under magnetic field or circular polarized light.[5–11] A capacitor-type device with thin-film TIs has been proposed for exciton condensates wherein quasi-particle excitation carries fractional charge.[12,13] TIs have attracted considerable attention in both scientific and technical application fields. One of the interesting challenges regarding the technical application of TIs is the artificial and transient tuning of their electronic properties. The modification of electronic bandgaps at the surface and in the bulk of TIs has been demonstrated with static methods that use dopants or the application of pressure.[13–16] However, the artificial and transient modification of bandgaps[12,13] in TIs via photoexcitation has not thus far been examined. The bulk bandgap of a TI, e.g., Bi$_2$Te$_3$, has been characterized as a direct gap at cryogenic temperatures, which is "buried" by the indirect gap formed at room temperature.[17] Therefore, the temperature dependence of the Bi$_2$Te$_3$ bandgap from cryogenic temperatures to room temperature is large. However, the temperature dependence of the indirect bandgap in Bi$_2$Te$_3$ above room temperature is negligibly small (see Fig. S1 of the supplementary material[18]). In this context, the responses of TIs under photoexcitation should be useful not only in understanding the nature of the electronic energy excitation and relaxation pathways but also in utilizing the ensuing photoinduced atomic displacements as a means to modify the electronic properties. The electronic dynamics in TIs under interband photoexcitation have been investigated with time- and angle-resolved photoelectron spectroscopy (tr-ARPES)[19,20] and time-resolved mid-infrared (MIR) spectroscopy.[21] The electrons photoexcited beyond the bandgap are immediately scattered into the bulk conduction band and partially into the surface state. The electrons in the bulk conduction band persistently relax into the bulk valence band through the surface state. A recent report has suggested that the balance between electrons and holes on the surface of TIs can strongly affect the electronic band structure of the system.[22] In contrast, coherent phonons have been observed in both the bulk and surface state of TIs under relatively weak photoexcitation.[23,24] The correlation of the electronic state dynamics to atomic motions under strong photoexcitation, particularly in the bulk, has not been considered in the dynamics of photoexcited TIs. Herein, we

a)Author to whom correspondence should be addressed. Electronic mail: hadamasaki@okayama-u.ac.jp

show that photoinduced atomic motions can be correlated to change in the electronic bandgap of TIs. We also examine the possibility of the artificial modification of the electronic structure in Bi_2Te_3 by interband photoexcitation via atomic motions occurring along the excited state surface.

II. EXPERIMENTAL MATERIALS AND METHODS

Near-ultraviolet (NUV) (3.1 eV) pump and MIR (0.12–0.22 eV) probe experiments were performed in the reflection mode on a Bi_2Te_3 bulk single-crystal. The experimental details of this optical pump-probe setup are presented elsewhere.[25] The incident angle of the pump and probe light was set nearly parallel to the surface normal of the sample. The pulse durations of the NUV and MIR pulses were 100 fs and <1 ps, respectively. The repetition rate and the incident fluence of the NUV pump pulse were 500 Hz and 1.7 mJ/cm^2, respectively. The absorption pump fluence (F_A) was calculated to be 1.0 mJ/cm^2, and the reflectivity of Bi_2Te_3 was measured to be 41%.

Time-resolved electron diffraction (Tr-ED) measurements were next performed in the transmission mode. The experimental setup of the compact DC-accelerated electron diffraction is provided elsewhere.[26] NUV light (3.1 eV) was focused to a 280-μm spot size on a single-crystalline Bi_2Te_3 ultrathin film (30 nm thick). The incident laser fluence was 0–9.0 mJ/cm^2. From the transmission and reflectivity of the Bi_2Te_3 thin film measured to be 15% and 41%, respectively, F_A was determined to be 0–4.0 mJ/cm^2. The acceleration voltage of the probe electron pulses was 75 keV under a DC electric field. Photoinduced structural changes inside the material were investigated with electron pulses containing 1.25×10^4 electrons confined to a 100-μm-diameter spot incident on the Bi_2Te_3 sample. The pulse duration of the electron beam was <1.5 ps as measured by the plasma method.[27] Diffracted and directly transmitted electrons were focused with a magnetic lens onto a 1:2 fiber-coupled charge-coupled device (CCD) camera (iKon-L HF, Andor) coated with a P43 (Gd_2O_2S:Tb) phosphor scintillator. To acquire one electron diffraction image, $1–4 \times 10^4$ shots of electron pulses were collected at repetition rates of 1 kHz below the F_A value of 2 mJ/cm^2 and 500 Hz above the F_A value of 2 mJ/cm^2 to avoid sample damage and accumulation of heat. The literature[28,29] indicates that the carrier dynamics of this class of topological insulator in 30-nm-thick-film correspond to that of a bulk sample rather than the surface of a sample. In the following discussion, we consider the Bi_2Te_3 ultrathin film to be a bulk sample.

N-type Bi_2Te_3 single crystals were grown by means of the modified Bridgman technique, as described in Ref. 6. The carrier density of the sample was found to be 5×10^{18} cm^{-3}. The surface of the bulk Bi_2Te_3 single crystal was cleaved with Scotch™ tape, and a fresh surface c-axis was used for the optical experiments. For the Tr-ED studies, the Bi_2Te_3 single crystal was cut to a 30-nm thickness perpendicular to the c-axis with a diamond knife on a microtome (UC7, Leica). The ultrathin Bi_2Te_3 film was "picked-up" with a commercial Cu TEM (#400) grid.

First-principles calculations within the framework of density functional theory (DFT) were performed with the

use of the full-potential linearized augmented plane-wave (FP-LAPW) method with the generalized gradient approximation/Perdew–Burke–Ernzerhof functional (GGA/PBE) implemented in the WIEN2k code.[30] Spin-orbit coupling was included as a second variation step. In order to describe the photoexcited states of Bi_2Te_3, the original rhombohedral crystal structure[31] was converted to orthorhombic symmetry ($a = 14.3362$ Å, $b = 57.5988$ Å, $c = 8.277$ Å) with the space group B2 (origin choice 5). The atomic coordinates at 0, 10, and 100 ps used for the calculations are listed in Tables S1–S7.[18] These coordinates were measured by time-resolved electron diffraction. The plane-wave cutoff energy was set to $R_{MT}K_{max} = 9$, where $R_{MT} = 2.5$ for both Bi and Te. The Brillouin zone was sampled with the Monkhorst–Pack scheme[32] with a Γ-centered $35 \times 6 \times 35$ k-point mesh, which achieved reasonable convergence (<1 meV) of the total energy and the bandgap.

III. RESULTS

A. NUV pump and MIR probe reflection spectroscopy

NUV pump and MIR probe reflective spectroscopy were used to characterize the carrier dynamics on the relevant time scales. Figure 1(a) presents the differential reflectivity ($\Delta R/R$) as a function of the probe photon energy at various time delays. As shown in Figs. 1(a) and 1(b), the signature of $\Delta R/R$ changes at a probe photon energy of approximately 0.13 eV. The decrease and recovery time constants in the
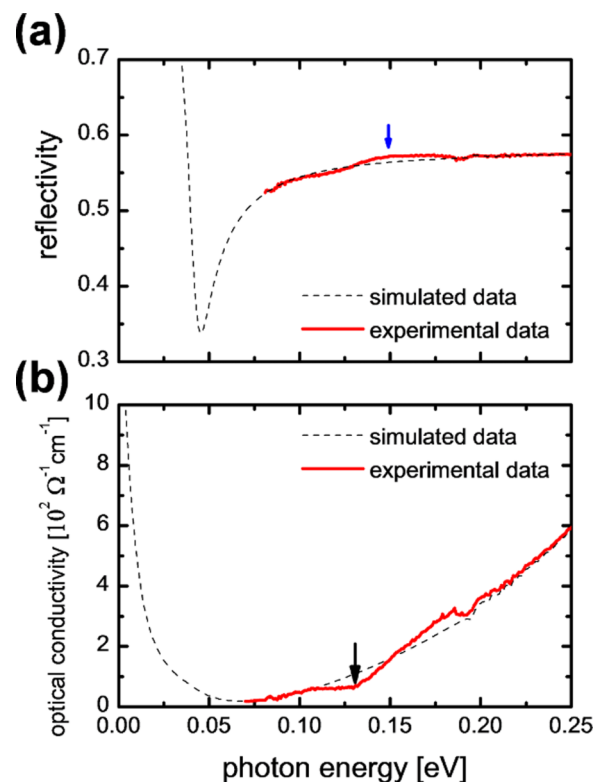

FIG. 1. (a) Two-dimensional plot of the normalized reflectivity as a function of probe photon energy at various time delays. (b) Typical time-resolved reflectivity $\Delta R/R$ at probe photon energies below (0.125 eV) and above (0.18 eV) the bandgap.

transient reflectivity from Bi_2Te_3 vary from 10 to 3 ps and 60 to 15 ps, respectively, in the probe photon energy range of 0.12–0.22 eV (Fig. S2 provides more detail on the decrease and recovery time constants[18]). When the ground-state electrons undergo direct excitation to the far-from-equilibrium state, holes are created at the edge of the bulk valence band, and the electrons in the surface state recombine into the bulk valence band to "fill" the holes. The excited electrons are scattered into the edge of the bulk conduction bands and then relaxed into the bulk valence band through the surface state. The variation in the time constants in the probe energy as shown in Figs. 1(a) and 1(b) reflects carrier dynamics in the surface state in a manner similar to that explained in Ref. 21.

The indirect bandgap of Bi_2Te_3 was confirmed to be 0.13 eV by transmission spectroscopy (Fig. S1[18]) and an optical conductivity spectrum calculated using the Kramers–Kronig (K–K) transform of the reflectivity (Figs. 2(a) and 2(b)). For the K–K transformation, we measured reflectivity in the energy range of 0.07–2.4 eV (see Fig. S3[18]) and assumed simulated reflectivity obtained using the conventional Drude model below 0.07 eV and ω^2 extrapolation above 2.4 eV. The figure shows a "bump" structure in the reflectivity spectrum at 0.14–0.15 eV (blue arrow). We obtained more details on this structure when we plot the simulated data based on the simple Drude model (dashed line). A comparison between the optical conductivity spectra calculated with the K–K transform from the experimental and simulated data reveals a kink structure (blue arrow in Fig. 2(b)) that is related to the bump structure in reflectivity. For the low-energy extrapolation method, we examined several models and parameters, but we could not find significant differences with respect to the position of the kink structure in the optical conductivity spectra shown in Fig. 2(b). The reflectivity spectrum modulation on the time scale of the first 10 ps is particularly noteworthy. Figure 3 presents the transient reflectivity in the probe-photon energy range of 0.12–0.22 eV. From the K–K analysis results, we note that the bandgap of Bi_2Te_3 is strongly related to the kink structure (0.14–0.15 eV), indicated by blue arrows in Figs. 2(a) and 3. This kink structure, marked in Fig. 3, is clearly shifted toward a lower energy (10 meV) in the time-resolved spectra. The penetration depth of the MIR light in Bi_2Te_3 is 400 nm (above the bandgap) and 700 nm (below
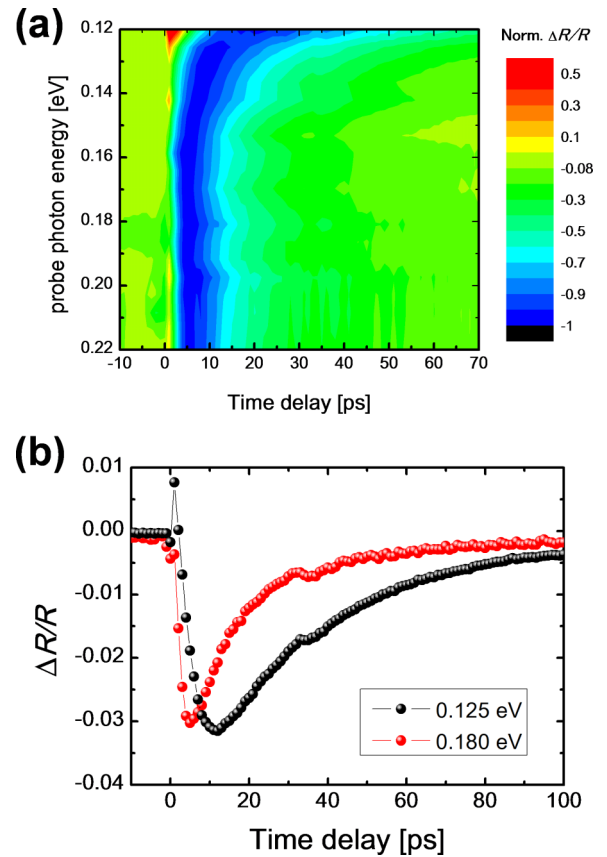

FIG. 2. (a) Mid-infrared reflectivity spectrum. The blue arrow indicates the bump positions. The simulated data (black dashed line) exhibit reflectivity without the kink structure. (b) The optical conductivity calculated using the K–K transformation of the reflectivity spectrum. The red solid line and black dashed line represent the experimental and simulated data, respectively. The black arrow indicates the bandgap energy.

the bandgap), whereas that of NUV light is approximately 30 nm, which is considerably different.[33–35] This mismatch of the penetration depth may affect the spectral shape of the reflectivity of the photoinduced state, however, we could not consider the effect of the mismatch on the pump-probe results because of the ambiguity of the spectral shape of the photoinduced state as well as the relatively small dispersion of the penetration depth in the photon energy range of our measurement. At present, we believe the observed shift of
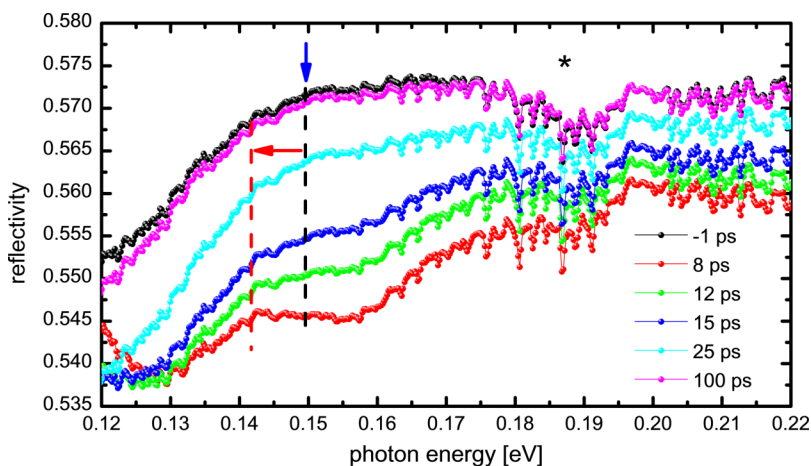

FIG. 3. Time evolution of the reflectivity from photoexcited Bi_2Te_3. The black and red dotted lines are visual guides showing the kink structure and the transient bandgap narrowing, respectively, as indicated by arrows. The symbol (*) indicates the mid-infrared absorption by water.

the kink structure in the reflectivity spectrum suggests the band-gap narrowing on the time scale of 10 ps. We present more detailed observations of the photoinduced dynamics on the results of the time-resolved electron diffraction.

B. Time-resolved electron diffraction measurements

We performed Tr-ED experiments that provided direct structural information on the evolution of the atomic configuration.[26,36–38] Figures 4(a) and 4(b) show an electron diffraction pattern from the 30-nm-thick $\langle 0001 \rangle$-oriented Bi_2Te_3 single-crystalline film and a simulated diffraction pattern obtained with the WinHREM™ software (based on the dynamical diffraction theory with multislice methods[39]), respectively. We analyzed the most significant diffraction spots. The resulting Tr-ED intensities are presented in Figs. 5(a)–5(c) for the $\{1\bar{2}10\}$ and $\{3\bar{3}00\}$ Bragg reflections from the Bi_2Te_3 film photoexcited at an F_A value of 1.5 mJ/cm^2. All the Tr-ED intensities are shown in Fig. S4.[18] The Tr-ED intensities shown in Figs. 5(a) and 5(b) are the products of three contributions: Debye–Waller effects, acoustic phonons, and atomic displacements within the unit cell. The intensity of the electron diffraction (I) can be expressed via the following equation:[40–42]

$$I = |G(\boldsymbol{K})|^2 \left| \sum_{j=1}^{M} f_j(\boldsymbol{K}) D_j(\boldsymbol{K}) \exp(2\pi i \boldsymbol{K} \cdot \boldsymbol{r}_j) \right|^2, \quad (1)$$

where $\boldsymbol{K}$ is the scattering vector, $G(\boldsymbol{K})$ is the Laue function, $f_j(\boldsymbol{K})$ is the atomic scattering factor, $D_j(\boldsymbol{K})$ is the Debye–Waller factor, and $\boldsymbol{r}_j$ is the equilibrium position of the jth atom in the unit cell. Because the intensity modulation by the acoustic phonon is derived from the mismatch of the Bragg condition, the contribution of the acoustic phonon is only related to ($G(\boldsymbol{K})$). On the other hand, the thermal effects and the effects of atomic displacements within the unit cell yield inversion-symmetric modulation in the electron diffraction intensity. The resulting temperature rise can be independently calculated from the thermal expansion coefficients $(1.3 \times 10^5 \text{ K}^{-1})$[43,44] and the shifts of the spot positions in the electron diffraction pattern (Fig. 5(d)). The value of the temperature rise from thermal expansion at 100 ps was calculated to be 100 K and to reach approximately 200 K on the time scale of nanoseconds. This temperature increase was

also indicated by the diffuse scattering background[45,46] (see Fig. S5[18]). The Debye–Waller factor can be expressed as a function of the mean square displacement (U_j) as follows:

$$D_j(\boldsymbol{K}) = \exp(-8\pi^2 |\boldsymbol{K}|^2 U_j). \quad (2)$$

The isotropic thermal displacement (U) can be calculated using the coefficient of linear contraction (ρ), which is derived from the bulk modulus,[44] and the atomic distance ($d_A = 4.38$ Å) with the following equation:[47,48]

$$U = \frac{k_B T}{d_A \rho}, \quad (3)$$

where k_B and T are the Boltzmann constant and lattice temperature, respectively. Taking into account the room temperature of 300 K, the temperature rise of approximately 100 K corresponded to decreases in the electron diffraction intensity of 1% and 3% of their original values for the $\{1\bar{2}10\}$ and $\{3\bar{3}00\}$ reflections.

Acoustic phonon vibrations at a frequency of 35 GHz (Fig. 5(e)) were also observed in the intensity of the diffraction spot from the $\{1\bar{2}10\}$ planes. In general, the sound velocity in a crystal is calculated as a function of the frequency of the acoustic phonon vibrations and film thickness.[49,50] In this study, the frequency of the acoustic mode (35 GHz) and film thickness (30 nm) yielded a sound velocity of 2100 m/s, which corresponds to the longitudinal-mode sound velocity (2000–2200 m/s) in Bi_2Te_3.[51,52] Since these acoustic phonon modulations have opposite phases in opposite planes, this effect of the acoustic phonons in the transient electron intensity can be canceled out by adding these opposite-phased oscillations. The remaining inversion six-symmetric contribution is attributed to the atomic displacements in the unit cell. As shown in Figs. 5(a) and 5(b), there is a two-step change: a decrease in the Tr-ED intensity by 5%–6% during the first 10 ps, and a subsequent gradual recovery over 10–100 ps. The symmetric-atomic-displacement-related component in the intensity of the higher-order diffraction spot $\{3\bar{3}00\}$ exhibits a 25% initial drop and a slight subsequent recovery (Fig. 5(c)).

To determine the transient atomic coordinates in the photoexcited Bi_2Te_3 crystal, we performed model calculations with the simulation package WinHREM. The electron pulses pass through the sample, parallel to the c-axis of the Bi_2Te_3
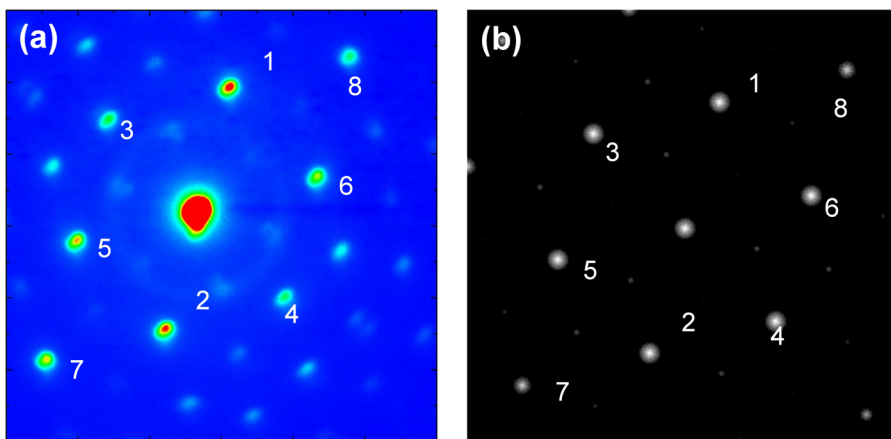

FIG. 4. (a) Typical electron diffraction pattern from Bi_2Te_3 thin films. (b) Electron diffraction pattern from Bi_2Te_3 simulated with the software WinHREM based on dynamic theory.
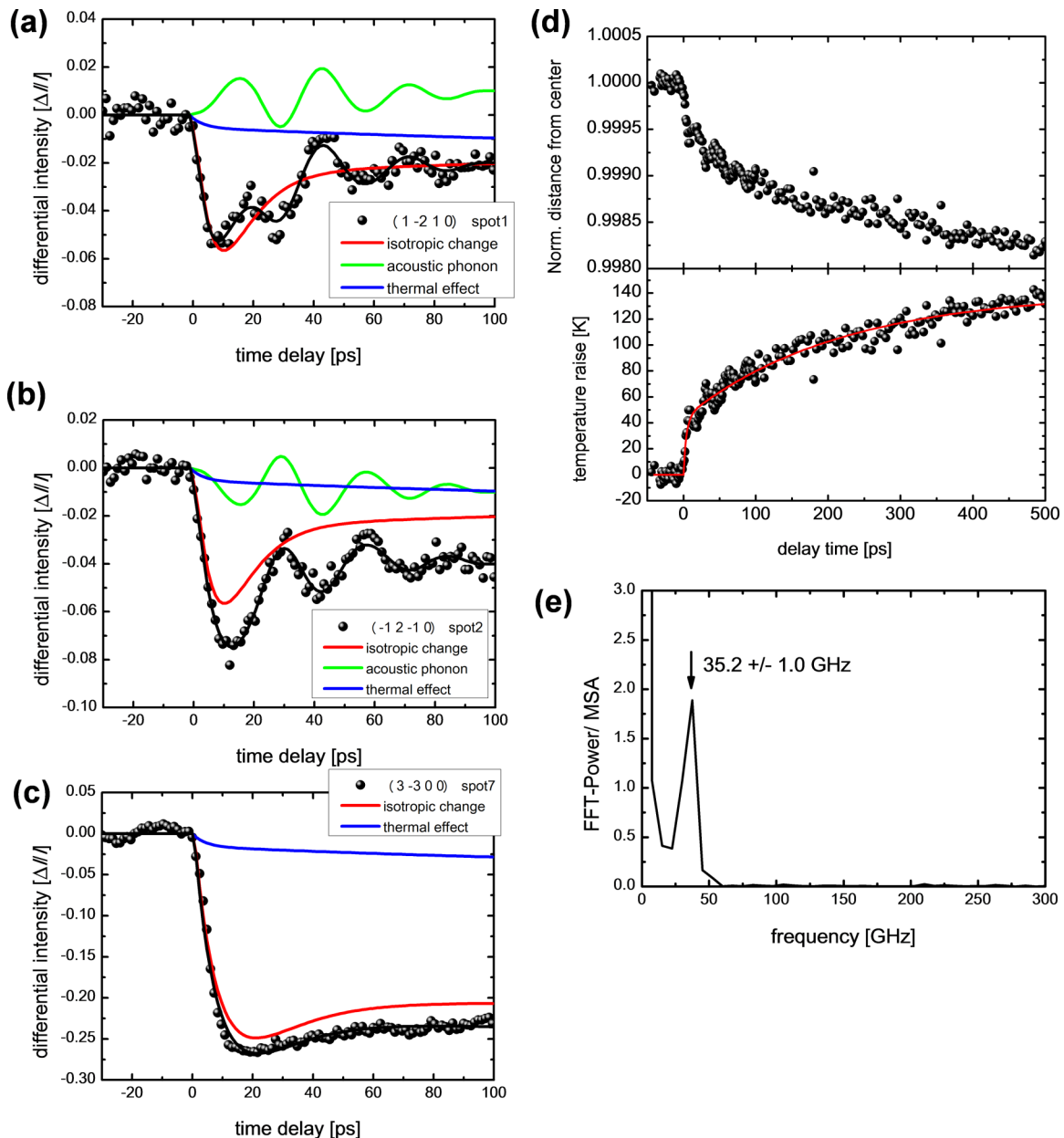
FIG. 5. (a)–(c) The time evolution of the electron diffraction intensity from $\{1\bar{2}10\}$ planes corresponding to spots 1 and 2 and that from $\{3\bar{3}00\}$ plane corresponding to spot 7 at $F_A = 1.5$ mJ/cm^2. The solid blue, green, and red lines indicate the contributions of the Debye–Waller thermal effect, acoustic phonon, and symmetric atomic displacement, respectively. (d) The peak shift of the $\{1\bar{2}10\}$ spots positions in the time-resolved electron diffraction experiments and temperature rise. The lattice constant of the undisturbed $\{1\bar{2}10\}$ plane is 0.2192 nm. (e) The Fourier transform of the acoustic phonon contribution. The blue lines in (a)–(c) were obtained independently from the red line in (d) and Eq. (2). To obtain the red lines in (a)–(c), double exponential fitting curves were fitted to the summations of the intensities of $\{1\bar{2}10\}$ diffraction spots minus the blue lines. The green lines in (a) and (b) were obtained by fitting exponentially increasing and decreasing oscillating equations to the raw data after subtraction of the red and blue lines. The black lines in (a)–(c) are the sum totals of the red, blue, and green lines.

crystal; therefore, the contributions along the *c*-axis (see Fig. S6[18]) are responsible for significant uncertainty in the determination of the disordered atomic coordinates. For the purpose of this discussion, we used the diffraction spots from the $\{1\bar{2}10\}$ and $\{3\bar{3}00\}$ planes. In principle, two atomic coordinates in the *ab* plane can be determined with two independent diffraction spots. A quintuple layer (QL), known as a functional periodic unit of this class of TIs, consists of five atomic layers (Te^1, Bi, Te^2, Bi, and Te^1). The Te^1 atom occupies a different site than the Te^2 atom from a crystallographic viewpoint. We assumed center-symmetric

motions of Bi and Te^1 atoms toward or away from the center axis of the unit cell with fixing of the Te^2 atom. Simulations based on dynamic theory were performed by changing the atomic coordinates of the Bi and Te^1 atoms. The calculations yielded differential electron diffraction intensities from the $\{1\bar{2}10\}$ and $\{3\bar{3}00\}$ planes as Bi atoms moved in relation to the Te^2 atoms upon fixing of the Te^1 atoms (Fig. S7(a)) and movement of the Te^1 atoms in relation to the Te^2 atoms with fixing of the Bi atoms (Fig. S7(b)).[18] The intensities of the diffraction spots decrease as the Bi atoms move; however, the motion of the Te^1 atoms makes no significant

contribution to the intensities of the diffraction spots. Thus, the first-step changes observed in Figs. 5(a) and 5(b) (10 ps) were concluded to have been induced primarily by the motions of the Bi atoms. For the purpose of further elaboration of the atomic displaced coordinates, the two-step changes in the diffraction intensity were characterized (Figs. S7(c) and S7(d)).[18] Transient atomic coordinates were determined to minimize $R^2(d_{Bi}, d_{Te})$ as expressed by the following equation:

$$R^2(d_{Bi}, d_{Te}) = \sum_i \left| \frac{I_{i,exp} - I_{i,sim(dBi,dTe)}}{I_{i,exp}} \right|^2, \qquad (4)$$

where d_{Bi} and d_{Te} are the displacements of the Bi and Te^1 atoms, respectively, and $I_{i,exp}$ and $I_{i,sim}(d_{Bi}, d_{Te})$ are the

experimental and simulated electron diffraction intensities of the ith index (i.e., $\{1\bar{2}10\}$ and $\{3\bar{3}00\}$), respectively. Figures 6(a)–6(e) depict the $R^2(d_{Bi}, d_{Te})$ maps as functions of the displacements of the Bi and Te^1 atoms at the representative time delays. The local minimum of the map is the transient atomic position, and the displacements of the Bi and Te^1 atoms are summarized in Fig. 6(f). As the figure shows, the Bi and Te^1 atoms move independently, and the motion observed in the first 10 ps corresponds to large Bi ($\sim$8 pm) and small Te^1 ($\sim$2 pm) displacements toward or away from the center axis. The atomic motion over 10–100 ps is the Te^1 ($\sim$2 pm) motion along the same direction and reversal of the Bi ($\sim$2 pm) displacement. The directions of these motions correspond to the fundamental-mode E^1_g and E^2_g phonons
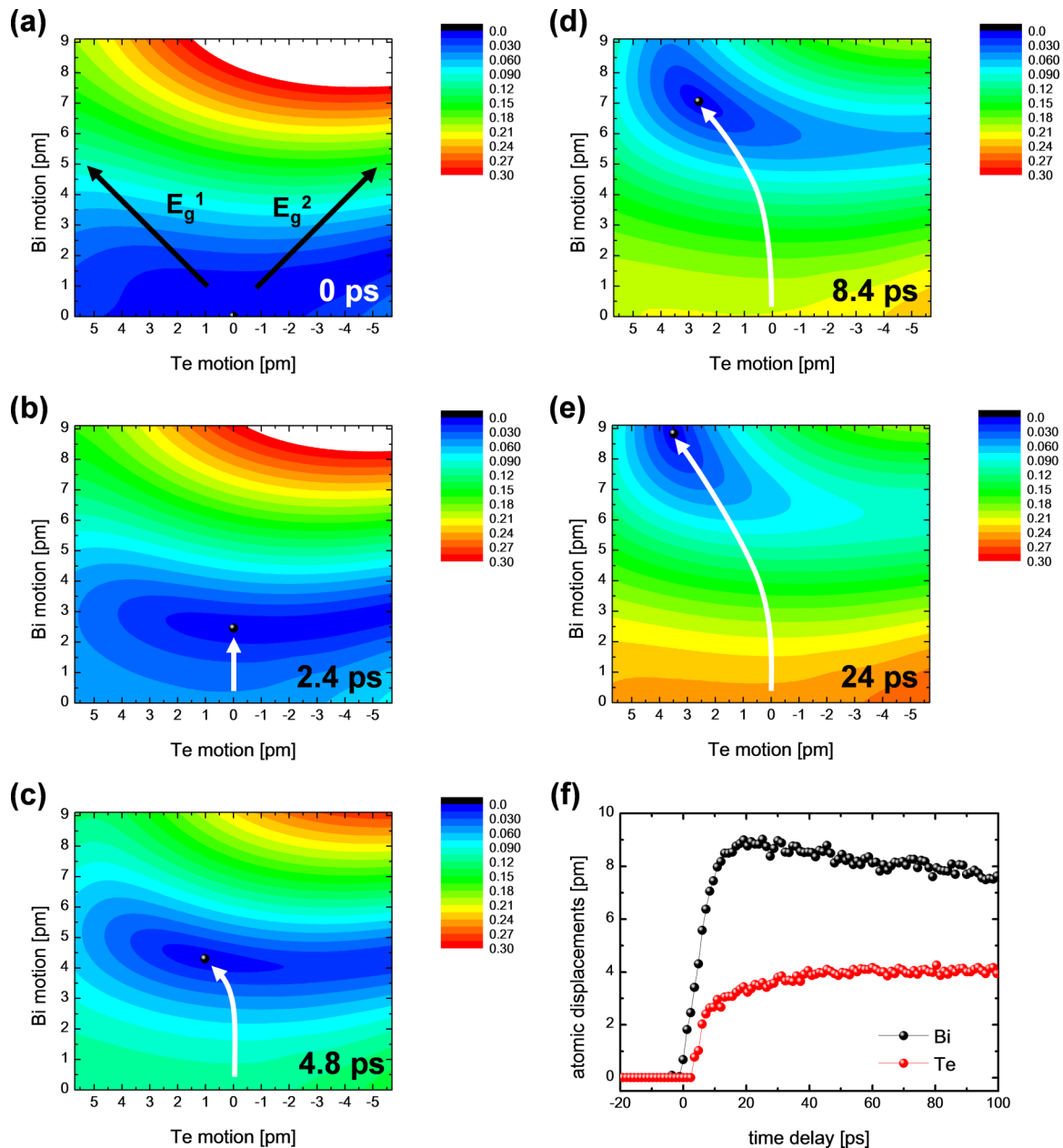

FIG. 6. Bi and Te^1 displacements derived from the time-resolved electron diffraction intensity and simulated electron diffraction intensity at (a) 0 ps, (b) 2.4 ps, (c) 4.8 ps, (d) 8.4 ps, and (e) 24 ps, respectively. The black arrows in (a) indicate the directions of motions of the E_g^1 and E_g^2 phonon modes. The white arrows in (b)–(e) indicate the motions of Bi and Te^1 atoms obtained from the analysis. (f) The displacements of Bi and Te^1 atoms from their original positions as a function of time delay.
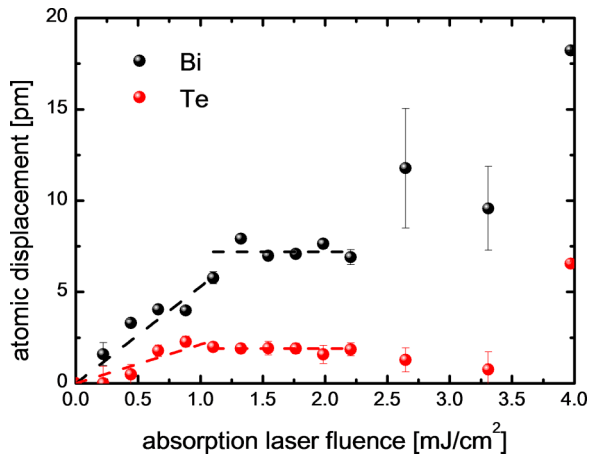
FIG. 7. The absorption laser fluence dependence on the atomic motions at the time delay of 10 ps.
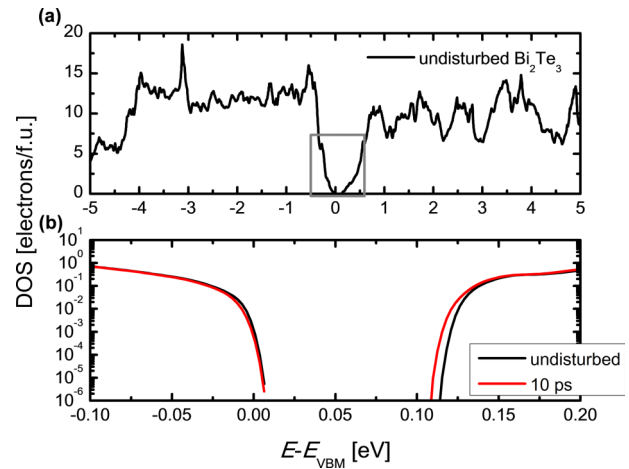

FIG. 9. (a) Density of states (DOS) calculated from unperturbed Bi_2Te_3. (b) Magnified view (gray box in (a)) of the DOS calculated from the displaced atomic coordinates obtained from the time-resolved electron diffraction.

(see Fig. S8).[18] These atomic displacements increase linearly with the absorption laser fluence at $F_A < 1.0$ mJ/cm^2 and are saturated at an F_A value of 1.0 mJ/cm^2. As shown in Fig. 7, the damage threshold of the ultrathin Bi_2Te_3 sample was determined to be 2.5 mJ/cm^2. In the F_A range from 1.0 to 2.0 mJ/cm^2, the atomic dynamics of Bi and Te are identical. The atomic displacements observed with Tr-ED are summarized in Fig. 8, along with the QL structure of Bi_2Te_3. The disordered atomic coordinates are listed in Tables S1–S7.[18]

IV. DISCUSSION

We discuss the correlation between the atomic motions and the change in the electronic structure of the Bi_2Te_3 system by comparing the results from the Tr-ED and NUV pump and MIR probe reflection spectroscopy. The transient electronic structure modulated by the disordered atoms can be calculated by DFT with the atomic coordinates obtained by Tr-ED. The DFT total energy increased by 1.0 meV per formula unit (f.u.) in 10 ps and relaxed to 0.2 meV/f.u. in 100 ps. These values correspond to excited electron densities of 4.5×10^{19} and $<1 \times 10^{19}$ cm^{-3}, respectively, in the bulk

conduction band where the photoexcited electron and hole density for NUV light is approximately 1×10^{21} e cm^{-3}. The density of the states obtained by the DFT calculation is shown in Figs. 9(a) and 9(b). The energy bandgap is 0.12 eV, which agrees with the spectroscopic measurements. The bandgap becomes approximately 5–10 meV narrower at 10 ps after photoexcitation. These results suggest that a fraction of the photoexcited and repopulated holes in the bulk valence band (around 5% of excited electrons and holes) create new atomic coordinates, which are related to the Bi motions occurring over 10 ps. These atomic motions cause bandgap narrowing, which is consistent with the NUV pump and MIR probe reflection spectroscopy results. Atomic displacements often reduce the crystal symmetry of a sample, which leads to the split of degenerated orbital level into several levels. This effect is called "crystal field splitting."[53,54] This crystal field splitting invokes the broadening of the conduction and valence bands, and results in bandgap narrowing unless the center value of the valence and conduction bands shifts. The bandgap renormalization effects[55] via hot electrons might also induce bandgap narrowing; however, these hot-electron
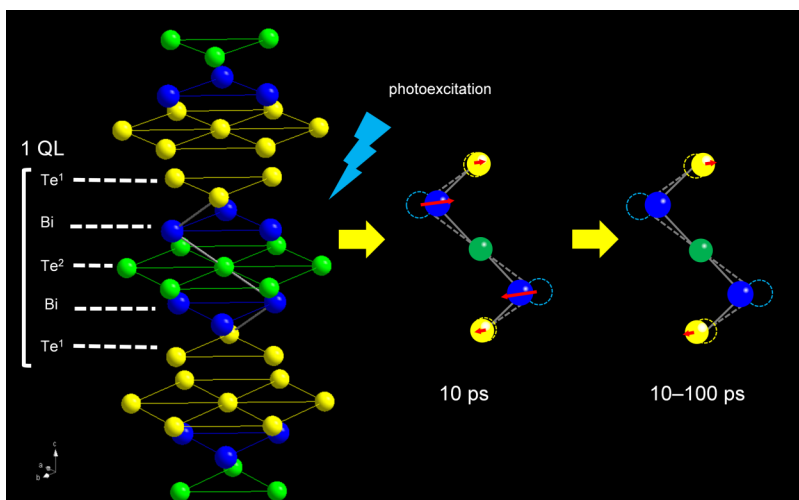

FIG. 8. Crystal structure of Bi_2Te_3. The quintuple layer (QL) consists of five atomic layers (Te^1, Bi, Te^2, Bi, and Te^1). The motions of Bi and Te^1 after the photoexcitation (10 ps and 100 ps) are indicated with the red arrows.

effects should start to occur within 3 ps when the hot electron is in the excited state. The time duration corresponding to the phenomena observed in our case was too large (10 ps) for the phenomena to be considered to be due only to hot-electron effects. Hot-hole effects[56] triggering these atomic motions can indirectly form one of the possible mechanisms for bandgap narrowing.

In summary, we observed that photoinduced atomic displacements in Bi_2Te_3 affect its bandgap, which is reflected in the DFT calculation. The observed dynamics illustrate the very nature of the photoexcited electronic relaxation pathways and the strong coupling between the electronic structure and atomic configuration of TIs. Bulk bandgap modification of TI films with intra- and interband photoexcitation in the range from THz to UV could play an important role in newer TI applications, particularly for modulating their properties on ultrafast time scales. To better understand electron–lattice coupling in TIs, it would be useful to observe the atomic motions along the *c*-axis with the use of ultrabright X-ray diffraction and spectroscopic methods.[57,58] As computing methods to calculate the excited states of these complex materials are further developed, *ab initio* molecular dynamics will also provide a more detailed microscopic understanding of these electronically coupled atomic motions.[59] In the present context, we have characterized both the transient electronic structure and atomic motions involved in photoinduced bandgap changes and demonstrated a causal connection to the atomic motions' amenable control. The tabletop combination of time-resolved MIR spectroscopy and electron diffraction methodologies can provide significant insight into material science and condensed matter physics in strongly correlated materials, or even in chemistry, where information on electronic and atomic dynamics is important for designing new functional materials.[60,61]

ACKNOWLEDGMENTS

[1]L. Fu and C. L. Kane, "Topological insulators with inversion symmetry," Phys. Rev. B **76**, 045302 (2007).

[2]D. Hsieh *et al.*, "A topological Dirac insulator in a quantum spin Hall phase," Nature **452**, 970 (2008).

[3]H. Zhang *et al.*, "Topological insulators in Bi_2Se_3, Bi_2Te_3 and Sb_2Te_3 with a single Dirac cone on the surface," Nat. Phys. **5**, 438 (2009).

[4]Y. L. Chen *et al.*, "Experimental realization of a three-dimensional topological insulator, Bi_2Te_3," Science **325**, 178 (2009).

[5]D.-X. Qu, Y. S. Hor, J. Xiong, R. J. Cava, and N. P. Ong, "Quantum oscillations and hall anomaly of surface states in the topological insulator Bi_2Te_3," Science **329**, 821 (2010).

[6]Y. L. Chen *et al.*, "Massive Dirac fermion on the surface of a magnetically doped topological insulator," Science **329**, 659 (2010).

[7]P. Cheng *et al.*, "Landau quantization of topological surface states in Bi_2Se_3," Phys. Rev. Lett. **105**, 076801 (2010).

[8]J. W. McIver, D. Hsieh, H. Steinberg, P. Jarillo-Herrero, and N. Gedik, "Control over topological insulator photocurrents with light polarization," Nat. Nanotechnol. **7**, 96 (2012).

[9]T. Kondo *et al.*, "Anomalous dressing of Dirac fermions in the topological surface state of Bi_2Se_3, Bi_2Te_3, and Cu-doped Bi_2Se_3," Phys. Rev. Lett. **110**, 217601 (2013).

[10]Y. Onishi *et al.*, "Ultrafast carrier relaxation through Auger recombination in the topological insulator $Bi_{1.5}Sb_{0.5}Te_{1.7}Se_{1.3}$," Phys. Rev. B **91**, 085306 (2015).

[11]Y. H. Wang, H. Steinberg, P. Jarillo-Herrero, and N. Gedik, "Observation of Floquet-Bloch states on the surface of a topological insulator," Science **342**, 453 (2013).

[12]B. Seradjeh, J. E. Moore, and M. Franz, "Exciton condensation and charge fractionalization in a topological insulator film," Phys. Rev. Lett. **103**, 066402 (2009).

[13]S.-Y. Xu *et al.*, "Topological phase transition and texture inversion in a tunable topological insulator," Science **332**, 560 (2011).

[14]S.-Y. Xu *et al.*, "Hedgehog spin texture and Berry's phase tuning in a magnetic topological insulator," Nat. Phys. **8**, 616 (2012).

[15]T. Sato *et al.*, "Direct evidence for the Dirac-cone topological surface states in the ternary chalcogenide $TlBiSe_2$," Phys. Rev. Lett. **105**, 136802 (2010).

[16]K. Kirshenbaum *et al.*, "Pressure-induced unconventional superconducting phase in the topological insulator Bi_2Se_3," Phys. Rev. Lett. **111**, 087001 (2013).

[17]G. A. Thomas *et al.*, "Large electronic-density increase on cooling a layered metal: Doped Bi_2Te_3," Phys. Rev. B **46**, 1553 (1992).

[18]See supplementary material at http://dx.doi.org/10.1063/1.4955188 for supplementary Figure S1 which shows infrared transmittance spectra from Bi_2Te_3 at temperatures of 287 K and 390 K. In Figure S2, we indicate the time constant of the decrease and recovery in the mid-infrared probe reflectance spectroscopy. Figure S3 shows the infrared-to-visible reflectivity spectrum at room temperature. Figure S4 shows that the time evolution of the electron diffraction intensity from the $\{1\bar{2}10\}$ planes corresponds to spot 1–6 and that the time evolution from the $\{3\bar{3}00\}$ planes corresponds to spots 7 and 8. Figure S5 shows the time-resolved change in the diffuse scattering background. Figure S6 shows the time-resolved electron intensity from the $(20\bar{2}10)$ diffraction plane. Figure S7 shows atomic displacements derived from the time-resolved electron diffraction. Figure S8 shows the Raman spectrum and the coherent phonon vibrations determined from the conventional near-IR pump-probe experiment. Tables S1–S7 present the atomic coordinates obtained from the time-resolved electron diffraction.

[19]J. A. Sobota *et al.*, "Ultrafast optical excitation of a persistent surface-state population in the topological insulator Bi_2Se_3," Phys. Rev. Lett. **108**, 117403 (2012).

[20]M. Hajlaoui *et al.*, "Time resolved ultrafast ARPES for the study of topological insulators: The case of Bi_2Te_3," Eur. Phys. J.: Spec. Top. **222**, 1271 (2013).

[21]C. W. Luo *et al.*, "Snapshots of Dirac fermions near the Dirac point in topological insulators," Nano Lett. **13**, 5797 (2013).

[22]M. Hajlaoui *et al.*, "Tuning a Schottky barrier in a photoexcited topological insulator with transient Dirac cone electron-hole asymmetry," Nat. Commun. **5**, 3003 (2014).

[23]J. A. Sobota *et al.*, "Distinguishing bulk and surface electron-phonon coupling in the topological insulator Bi_2Se_3 using time-resolved photoemission spectroscopy," Phys. Rev. Lett. **113**, 157401 (2014).

[24]K. Norimatsu *et al.*, "Dynamics of all the Raman-active coherent phonons in Sb_2Te_3 revealed via transient reflectivity," J. Appl. Phys. **117**, 143102 (2015).

[25]N. Fukazawa *et al.*, "Time-resolved infrared vibrational spectroscopy of the photoinduced phase transition of $Pd(dmit)_2$ salts having different orders of phase transition," J. Phys. Chem. C **117**, 13187 (2013).

[26]M. Hada *et al.*, "Cold ablation driven by localized forces in alkali halides," Nat. Commun. **5**, 3863 (2014).

[27]M. Hada, K. Pichugin, and G. Sciain, "Ultrafast structural dynamics with table top femtosecond hard x-ray and electron diffraction setups," Eur. Phys. J.: Spec. Top. **222**, 1093 (2013).

[28]D. Hsieh *et al.*, "Selective probing of photoinduced charge and spin dynamics in the bulk and surface of a topological insulator," Phys. Rev. Lett. **107**, 077401 (2011).

[29]Y. D. Glinka *et al.*, "Ultrafast carrier dynamics in thin-films of the topological insulator Bi_2Se_3," Appl. Phys. Lett. **103**, 151903 (2013).

[30]P. Blaha, K. Schwarz, P. Sorantin, and S. B. Trickey, "Full-potential, linearized augmented plane wave programs for crystalline systems," Comput. Phys. Commun. **59**, 399 (1990).

[31]S. Nakajima, "The crystal structure of $Bi_2Te_{3-x}Se_x$," J. Phys. Chem. Solids **24**, 479 (1963).

[32]H. J. Monkhorst and J. D. Pack, "Special points for Brillouin-zone integrations," Phys. Rev. B **13**, 5188 (1976).

[33]H. Cui, I. B. Bhat, B. O'Quinn, and R. Venkatasubramanian, "*In-situ* monitoring of the growth of Bi_2Te_3 and Sb_2Te_3 films and Bi_2Te_3-Sb_2Te_3 superlattice using spectroscopic ellipsometry," J. Electron. Mater. **30**, 1376 (2001).

[34]A. Zimmer *et al.*, "Optical constants of electroplated Bi_2Te_3 films by Mueller matrix spectroscopic ellipsometry," Thin Solid Films **516**, 2922 (2008).

[35]A. Y. Morsy, S. S. Fouad, E. Hashem, and A. A. El-Shazly, "Optical properties of thermally deposited bismuth telluride in the wavelength range of 2.5–10 μm," Acta Phys. Pol., A **80**, 819 (1991).

[36]G. Sciaini and R. J. D. Miller, "Femtosecond electron diffraction: Heralding the era of atomically resolved dynamics," Rep. Prog. Phys. **74**, 096101 (2011).

[37]A. H. Zewail, "4D ultrafast electron diffraction, crystallography, and microscopy," Annu. Rev. Phys. Chem. **57**, 65 (2006).

[38]M. Gulde *et al.*, "Ultrafast low-energy electron diffraction in transmission resolves polymer/graphene superstructure dynamics," Science **345**, 200204 (2014).

[39]K. Ishizuka and N. Uyeda, "A new theoretical and practical approach to the multislice method," Acta Crystallogr., Sect. A **33**, 740 (1977).

[40]M. Hada, K. Okimura, and J. Matsuo, "Characterization of structural dynamics of VO_2 thin film on c-Al_2O_3 using in-air time-resolved x-ray diffraction," Phys. Rev. B **82**, 153401 (2010).

[41]L.-M. Peng, "Quasi-dynamical electron diffraction—A kinematic type of expression for the dynamical diffracted-beam amplitudes," Acta Crystallogr., Sect. A **56**, 511 (2000).

[42]S. Nie, X. Wang, J. Li, R. Clinite, and J. Cao, "Femtosecond electron diffraction: Direct probe of ultrafast structural dynamics in metal films," Microsc. Res. Tech. **72**, 131 (2009).

[43]L. M. Pavlova, Y. I. Shtern, and R. E. Mironov, "Thermal expansion of bismuth telluride," High Temp. **49**, 369 (2011).

[44]B.-L. Huang and M. Kaviany, "*Ab initio* and molecular dynamics predictions for electron and phonon transport in bismuth telluride," Phys. Rev. B **77**, 125209 (2008).

[45]R. Xu and T.-C. Chiang, "Determination of phonon dispersion relations by x-ray thermal diffuse scattering," Z. Kristallogr. **220**, 1009 (2005).

[46]M. J. Gutmann, G. Graziano, S. Mukhopadhyay, K. Refson, and M. von Zimmerman, "Computation of diffuse scattering arising from one-phonon excitations in a neutron time-of-flight single-crystal Laue diffraction experiment," J. Appl. Crystallogr. **48**, 1122 (2015).

[47]A. I. Frenkel and J. J. Rehr, "Thermal expansion and x-ray-absorption fine-structure cumulants," Phys. Rev. B **48**, 585 (1993).

[48]T. Sakuma *et al.*, "Correlation effects among thermal displacements of atoms in KBr," Solid State Ionics **192**, 54 (2011).

[49]G. Moriena, M. Hada, G. Sciaini, J. Matsuo, and R. J. D. Miller, "Femtosecond electron diffraction: Preparation and characterization of (110)-oriented bismuth films," J. Appl. Phys. **111**, 043504 (2012).

[50]M. Harb *et al.*, "Excitation of longitudinal and transverse coherent acoustic phonons in nanometer free-standing films of (001) Si," Phys. Rev. B **79**, 094301 (2009).

[51]L. W. da Silva and M. Kaviany, "Micro-thermoelectric cooler: Interfacial effects on thermal and electrical transport," Int. J. Heat Mass Transfer **47**, 2417 (2004).

[52]K. Hoefer *et al.*, "Intrinsic conduction through topological surface states of insulating Bi_2Te_3 epitaxial thin films," Proc. Natl. Acad. Sci. U. S. A. **111**, 14979 (2014).

[53]R. G. Shulman and K. Knox, "Interactions of p_σ and p_π orbitals in transition element fluorides," Phys. Rev. Lett. **4**, 603 (1960).

[54]R. G. Shulman and S. Sugano, "Calculation of the crystal field splitting," Phys. Rev. Lett. **7**, 157 (1961).

[55]J. Shah, R. F. Leheny, and C. Lin, "Dynamic Burstein shift in GaAs," Solid State Commun. **18**, 1035 (1976).

[56]P. W. Juodawlkis and S. E. Ralph, "Hole-induced transient bandgap renormalization: A mechanism for photo-induced absorption in defect-engineered semiconductors," Appl. Phys. Lett. **76**, 1722 (2000).

[57]K. J. Gaffney and H. N. Chapman, "Imaging atomic structure and dynamics with ultrafast x-ray scattering," Science **316**, 1444 (2007).

[58]R. J. D. Miller, "Femtosecond crystallography with ultrabright electrons and x-rays: Capturing chemistry in action," Science **343**, 1108 (2014).

[59]E. S. Zijlstra, A. Kalitsov, T. Zier, and M. E. Garcia, "Fractional diffusion in silicon," Adv. Mater. **25**, 5605 (2013).

[60]V. R. Morrison *et al.*, "A photoinduced metal-like phase of monoclinic VO_2 revealed by ultrafast electron diffraction," Science **346**, 445448 (2014).

[61]T. Ishikawa *et al.*, "Direct observation of collective modes coupled to molecular orbital–driven charge transfer," Science **350**, 1501 (2015).